Biomaterials Science

PAPER

View Article Online
View Journal

Cite this: DOI: 10.1039/c6bm00297h

In vivo biodistribution of stable spherical and filamentous micelles probed by high-sensitivity SPECT†

L. Jennings,*‡[a] O. Ivashchenko,*‡[b,c,d] I. J. C. Marsman,[b] A. C. Laan,[b] A. G. Denkova,[b] G. Waton,[a] F. J. Beekman,*[b,c] F. Schosseler*[a] and E. Mendes[e]

Received 29th April 2016,
Accepted 4th June 2016

DOI: 10.1039/c6bm00297h

www.rsc.org/biomaterialsscience

Understanding how nanoparticle properties such as size, morphology and rigidity influence their circulation time and biodistribution is essential for the development of nanomedicine therapies. Herein we assess the influence of morphology on cellular internalization, *in vivo* biodistribution and circulation time of nanocarriers using polystyrene-*b*-poly(ethylene oxide) micelles of spherical or elongated morphology. The glassy nature of polystyrene guarantees the morphological stability of the carriers *in vivo* and by encapsulating Indium-111 in their core, an assessment of the longitudinal *in vivo* biodistribution of the particles in healthy mice is performed with single photon emission computed tomography imaging. Our results show prolonged blood circulation, longer than 24 hours, for all micelle morphologies studied. Dynamics of micelle accumulation in the liver and other organs of the reticuloendothelial system show a size-dependent nature and late stage liver clearance is observed for the elongated morphology. Apparent contradictions between recent similar studies can be resolved by considering the effects of flexibility and degradation of the elongated micelles on their circulation time and biodistribution.

Introduction

Properties such as polymeric architecture, surface charge or size are known to be some of the main factors determining the behavior of nanoparticles both *in vitro* and *in vivo*. This knowledge is derived from a plethora of studies that have been performed using particles of spherical morphology. This is partially due to the simplicity of preparation and characterization of spherical particles as opposed to elongated ones. Indeed, the latter include all the complexities of the former while adding extra physical properties such as length, aspect ratio and flexibility, resulting in an intrinsically more complex system to develop, characterize and interpret. Therefore, the influence of morphology on the *in vivo* behavior of nanocarriers is, comparably, unexplored.

Nonetheless, in recent years theoretical and experimental studies have suggested the advantages of using oblate or high aspect ratio particles both *in vitro* and *in vivo*. Decuzzi *et al.* have shown through simulation that there exist an optimal aspect ratio for particles that maximizes adhesive strength to membranes.[1] Mitragotri *et al.* have shown that the morphology of polystyrene microparticles influences phagocytosis mechanisms and that elongated polystyrene nanoparticles target lungs and brain endothelium more efficiently than their spherical counterparts.[2,3]

The most remarkable results regarding the use of elongated carriers were shown by Geng *et al.* when exploiting the enhanced permeability and retention (EPR) effect.[4] This effect consists in the passive extravasation and retention of nanoparticles through the highly defective blood vessels which are formed as a consequence of the oxygen depletion and release of cytokines in the core of solid tumors.[5–8] In their pioneering work the authors showed that elongated poly(ethylene glycol)-*b*-poly(ε-caprolactone) filomicelles display circulation half-life time of up to five days. This result is orders of magnitude larger than what is generally defined as "long circulating nanoparticles" and it is of paramount importance for passive targeting systems as longer circulation increases the probability of

[a]*Institut Charles Sadron (CNRS), University of Strasbourg, Strasbourg, France. E-mail: laurence.jennings@ics-cnrs.unistra.fr*
[b]*Department of Radiation Science and Technology, Delft University of Technology, Delft, The Netherlands. E-mail: o.ivashchenko-1@tudelft.nl*
[c]*MILabs B.V., Utrecht, The Netherlands*
[d]*Department of Translational Neuroscience, Brain Center Rudolf Magnus, University Medical Center, Utrecht, The Netherlands*
[e]*Department of Chemical Engineering, Delft University of Technology, Delft, The Netherlands*

†Electronic supplementary information (ESI) available: *In vitro* characterization of the PS-PEO micelles, micelle radiolabeling efficiency, late stage biodistribution SPECT scans corresponding quantitative tables and animated maximum intensity projections of the SPECT/CT. See DOI: 10.1039/c6bm00297h

‡These authors contributed equally to the work.

passive uptake in the "target" areas. Although these authors concluded to a definitive advantage in using nanocarriers with large aspect ratio, their PEO-PCL filo-micelles undergo an elongated to spherical transition due to the hydrolytic degradation of the core forming block.[9] Since the filomicelles are only accumulating after they have decayed to a spherical morphology, this system does not provide any insight on the biodistribution of elongated objects. This can indeed be seen from their results where the only differences between the spherical PEO-PCL micelles and the filomicelles are in the drug loading efficiency and circulation time.[10]

Very recently Müllner *et al.*[11] investigated the circulation time and biodistribution of high aspect ratio, non-degradable, cylindrical polymer brushes of different stiffness and length. They showed that increasing length and stiffness reduce the circulation time and the accumulation in the spleen. Their results are profoundly different from those of the PCL filomicelles, suggesting a strong importance of stiffness in the biodistribution and circulation time of elongated nanoparticles. However, their study did not provide longitudinal data which is necessary for understanding the accumulation and the elimination pathways involved in the clearance of the nanocarriers.

Here we used longitudinal single photon emission computed tomography (SPECT) imaging to investigate the circulation, the biodistribution and the clearance of rigid model nanocarriers with spherical and cylindrical morphology to obtain a more complete picture of the effects of size and rigidity on these parameters. In order to do this, we used a model system of polystyrene-*b*-poly(ethylene oxide) micelles and studied *in vitro* and *in vivo* the effect of micelle morphology on their cellular uptake and biokinetics. In the PS-PEO micelles used, the strong hydrophobicity of the core forming block, polystyrene, and its high glass transition temperature eliminate the possibility of unimer exchange.[12] From the kinetic entrapment of the unimers within far from equilibrium supramolecular structures, the concept of non-ergodic micelles is derived.[13] These micelles do not evolve over time while in solution or during their circulation *in vivo*. This characteristic provides both stability and a higher degree of freedom on the possible morphologies that are obtainable with a certain copolymer.[14–16] Subsequently, a fluorescent dye was incorporated and the fluorescently labeled micelles were used for *in vitro* cellular uptake experiments. Finally, ^{111}In was encapsulated and the radiolabeled micelles were used for *in vivo* biokinetics studies by SPECT in healthy mice.

Experimental section

Materials

Poly(styrene-*b*-ethylene oxide) block copolymers $PS_{9.5k}$-PEO_{18k} (PDI = 1.09) and $PS_{9.5k}$-PEO_{5k} (PDI = 1.04) were purchased from (Polymer Source Inc., Canada), the subscripts indicate the molecular weight of the blocks in Dalton. Anhydrous chloroform ≥99%, 0.5–1% ethanol as stabilizer, fluorescent dye 1,1′-dioctadecyl-3,3,3′,3′-tetramethylindocarbocyanine perchlorate (DiI), Sephadex® G-25 and Fetal Bovine Serum (FBS), were purchased from Sigma Aldrich (Sigma-Aldrich Chemie B.V., The Netherlands). Sterile Phospate Buffered Saline (PBS), 0.25% trypsin-ethylenediaminetetraacetic acid (EDTA) and penicillin–streptomycin were purchased from Gibco (Fischer Scientific, The Netherlands). BioWhittaker Dulbecco's Modifed Eagle Medium (DMEM) and Ham's F10 were purchased from Lonza (Lonza Benelux B.V., The Netherlands). Vectashield-4′,6-diamidino-2-phenylindole (DAPI) was purchased from Vector Laboratories (Brunschwig Chemie, The Netherlands). Glass stirring bars, one cm long, were purchased from VWR (VWR International, France). Silicon substrates, 5 × 5 mm polished, were purchased from Siltronix (Siltronix B.V., France). The radioactive ^{111}In-chloride was provided by IDB Holland (IDB Holland B.V., The Netherlands). All the reagents were used as received unless stated otherwise.

Micelle formation

A stock solution was prepared by dissolving 10 mg mL^{-1} block copolymer in chloroform. A 100 μL aliquot of the stock solution was added to 2.3 mL of PBS. After this, an emulsion between the two immiscible solvents was formed by stirring using a glass coated magnetic stirring bar. The emulsion was stirred until complete evaporation of the chloroform.

Three different micelle types were prepared: two of spherical and one of elongated morphology. The spherical ones were formed using $PS_{9.5k}$-PEO_{18k}. By controlling the evaporation rate of the chloroform phase in the emulsion spherical micelles of two different diameters were obtained. The large spherical micelles, spherical polystyrene large micelles (sPSL), were formed by leaving the vial open during the evaporation stage. The small spherical micelles, spherical polystyrene small micelles (sPSS), were formed by maintaining the vial closed during the whole evaporation stage. Elongated micelles, elongated polystyrene small micelles (ePSS), were formed using $PS_{9.5k}$-PEO_{5k} and by keeping the vial closed during the evaporation stage.

Fluorescently labeled micelles were prepared by including fluorescent dye DiI directly to the stock solution in 0.02 wt% to copolymer weight.

Spherical micelle characterization

The intensity weighted particle size distribution and average hydrodynamic diameter of the spherical micelles were obtained by dynamic light scattering (DLS). Each micelle sample was diluted to a concentration of 0.1 mg mL^{-1} and measured using an ALV/DLS/SLS-5020F experimental setup (ALV Laser Vertriebsgesellshaft GmbH, Germany) with a He–Ne laser (14 mW, λ_0 = 632.8 nm), a compact ALV/CGS-8 Goniometer system, and an ALV-7002 autocorrelator at scattering angles from 20° to 120°. The CONTIN method was used for the analysis of the normalized autocorrelation functions of the scattered intensity.

Atomic force microscopy (AFM) was used to obtain topographic scans of the spherical micelles. Ten μL of micelle solu-

tion were spin coated onto 5 × 5 silicon substrates and these were imaged using an NTegra microscope (NT-MDT Co., Russia) in semi contact mode with an NSG03 cantilever (k = 1.7 N m^{-1}).

Elongated micelle characterization

The diameter and length of the elongated micelles was determined by Scanning Electron Microscopy (SEM). Droplets of 10 μL of micelle solution were diluted to 0.1 mg mL^{-1} and spin coated onto 5 × 5 mm silicon substrates. These were imaged using a SU8000 UHR Cold-Emission FE-SEM Scanning Electron Microscope (Hitachi, Japan). The samples were imaged at 1 kV acceleration voltage and without applying any conductive coating to the sample.

The diameter of the elongated micelles was also measured by AFM, using the same procedure and equipment as for the spherical micelles.

The length distribution of the elongated micelles was reduced using an Ultra Turrax IKA T10 basic homogenizer (IKA, Germany). Each sample of 2.3 mL was homogenized at 30k RPM for 30 seconds in total.

Radiolabeling

A solution of 2.3 mL PBS (pH 7.4) and 1 mM tropolone was prepared. The required amount of ^{111}In was added to this aqueous solution and stirred using a glass coated magnetic stirring bar for 5 minutes, allowing the formation of indium–tropolone complexes. After this, a 100 μL aliquot of polymer stock solution was added and an emulsion with water was formed by stirring the two immiscible solvents with a glass magnetic stirring bar. The emulsion was mixed until evaporation of chloroform.

Purification of the radiolabeled micelles from unencapsulated and uncomplexed tropolone and ^{111}In was performed by size exclusion chromatography using Sephadex® G-25 gel. Elution fractions were collected and the activity of each fraction was counted in a 2480 Wizard2 Automatic Gamma Counter (PerkinElmer Nederland BV, The Netherlands).

In vitro characterization of PS-PEO micelles

Details about *in vitro* model and cytotoxicity experiments setup are available in the ESI.†

In vivo characterization of PS-PEO micelles

Animal experiments were performed with C57Bl/6 mice according to protocols approved by the Animal Ethical Committee of the UMC Utrecht and in accordance with Dutch Law on Animal experimentation. SPECT/CT imaging was used as a noninvasive method to access circulation dynamics and tissue deposition of ^{111}In-labelled micelles.

Three study groups of two animals each were assigned for imaging with ^{111}In-sPSL, ^{111}In-sPSS or ^{111}In-ePSS micelles respectively. All animals were anesthetized with isoflurane (2% in air) and injected with activity *via* the tail vein. The average injected activities per study group were 1.45 MBq (1.5 mg) ^{111}In-sPSL, 0.26 MBq (1.8 mg) ^{111}In-sPSS and 0.42 MBq (1.5 mg) ^{111}In-ePSS respectively. After this, total body SPECT/CT scans of 30 minutes were acquired at 0 (just after the injection), 24 and 48 hours p.i.

To obtain more detailed information on the late-stage biodistribution of the compound in the spleen and the liver of the animals, additional 30 minutes acquisitions focused on the abdominal area were performed immediately after the end of the 48 hours p.i. total body SPECT/CT scans.

SPECT/CT imaging and data analysis

All animals were imaged in a U-SPECT+/CT scanner (MILabs B.V., The Netherlands).[17] The SPECT scans were acquired in a list-mode data format with an XUHS-2.0 mm mouse pinhole collimator.[18] After this, SPECT image reconstructions were carried out with a pixel-based order-subset expectation maximization (POSEM)[19] algorithm that included resolution recovery and compensation for distance-dependent pinhole sensitivity.[20] For the SPECT images in this paper, we used 4 subsets and 12 iterations image reconstruction with an isotropic 0.4 mm-voxel grid. Triple-energy-window based Compton scatter correction was performed according to King *et al.*[21] A 20% ^{111}In photopeak window was centered at 171 keV. Two background windows were placed on both sides of the photopeak window with a width of 4% of the photopeak, *i.e.* 6.8 keV each. Hereafter, non-uniform attenuation correction and absolute quantification of SPECT images was performed according to Wu *et al.*[22] For visual representation in the manuscript the reconstructed volumes of SPECT scans were post-filtered width three-dimensional Gaussian filter.

Corresponding CT scans were acquired with a tube setting of 55 kV and 615 μA. In total, 2 frames of 182 projections over 360° were acquired in step and shoot rotation mode. The acquired projection data was reconstructed using SkyScan NRecon software to generate a 3-D CT image on 0.1693 × 0.1693 × 0.1695 mm voxel grid.

To calculate the uptake of radiolabeled micelles in the organ of interest, the registered CT and quantified SPECT images were analyzed using PMOD 3.6 biomedical image analyzing software (PMOD, Switzerland). A three-dimensional region-of-interest (ROI) was manually drawn to encompass the radioactivity uptake in the organ of interest. Separate ROIs were drawn for the radioactivity uptakes in the heart, liver, spleen, brain, lungs, left and right kidneys, and the bladder. The uptake was expressed as % injected dose (%ID) per mL of tissue volume (%ID mL^{-1}). All quantification data was reported as mean ± standard deviation within one animal study group. Comparison of statistical correlation between the biodistribution of different nanocarriers was conducted using Pearson's correlation coefficient.

Results

Formation and characterization of PS-PEO micelles

Three types of micelles were used in this work: two spherical, of different diameters, and one elongated. The larger spherical micelles, sPSL, were obtained through a fast evaporation rate

(approximately 4 hours for 100 μL of chloroform in water), while the smaller ones, sPSS, were obtained by a slower more sustained evaporation rate (approximately 24 hours for 100 μL of chloroform in water). Similar effects of evaporation time on micelle morphology have been previously reported in the literature.[23] The formation of elongated micelles, ePSS, was only possible through a slow evaporation rate of the solvent. This is due to the different mechanism behind the formation of the spherical and elongated micelles which will be object of a separate study.

The spherical micelles were characterized by DLS, the hydrodynamic diameters obtained are taking into account the hydrated poly(ethylene-oxide) corona of the micelle. Due to their large size the elongated micelles could not be characterized using light scattering techniques, therefore it was necessary to use microscopy. The elongated micelle diameter was measured by SEM, however, due to the contrast being generated only by the more electronically dense polystyrene core, this measure does not take into account the presence of a PEO corona. In order to bridge the difference between DLS and SEM results, AFM has been used to measure the diameter of the micelles. The micelles used, with the corresponding forming copolymer and their size characterization performed by DLS, AFM and SEM, are reported in Table 1 and the AFM topography scans of the micelles are shown in Fig. 1.

The size obtained for the spherical micelles by AFM is consistent with the values obtained by DLS. The value obtained for the ePSS exceeds that obtained by SEM due to the contribution of the corona. We can conclude that since a direct comparison between scattering techniques and microscopy techniques is not possible, AFM is an appropriate technique for comparison of cross sectional dimensions of block copolymer micelles of different morphologies.

Fluorescence microscopy has been previously used to determine the length distribution of elongated micelles,[4] however, the resolution limit of optical microscopy prevents the distinction of anything smaller than the diffraction limit of visible light (approximately 200 nm). If the length distribution of elongated micelles would be determined by fluorescence microscopy it would appear shifted towards higher values by neglecting the contribution of the smaller micelles. In order to avoid this, SEM was used to determine the length of the micelles. As formed, the elongated micelles had a very broad length distribution that reached hundreds of microns. In order to make them suitable for *in vivo* applications, the micelles were shortened using a high power homogenizer. The strong shear stress applied during mixing fractured the micelles and resulted in a more narrow length distribution with an average length of 0.6 μm (Fig. 2).

In vitro cytotoxicity assay of PS-PEO micelles

The cytotoxicity of spherical PS-PEO micelles with various block copolymer molecular weights has been studied by D'Addio *et al.*[24] However, morphology-dependent cytotoxicity has been previously shown for carbon based, gold and hydroxyapatite nanoparticles.[25–27] Therefore, it was important to verify if the different morphologies used herein displayed different cytotoxic effects. This was determined using the water soluble tetrazolium assay (WST-1) on human cervical (HeLa) cells. The results are shown in Fig. S1 of the ESI.†

Table 1 List of the micelles used. The diameters of the two spherical micelles are hydrodynamic diameters obtained by DLS while the diameter and length of the elongated micelles were obtained by SEM measurements

Micelle type	Copolymer	Diameter [nm] DLS	Length [nm] AFM	SEM	SEM
sPSS	$PS_{9.5k}$-PEO_{18k}	106 ± 7	120 ± 21	—	—
sPSL	$PS_{9.5k}$-PEO_{18k}	170 ± 8	190 ± 32	—	—
ePSS	$PS_{9.5k}$-PEO_{5k}	—	92 ± 12	31 ± 3	600 ± 310

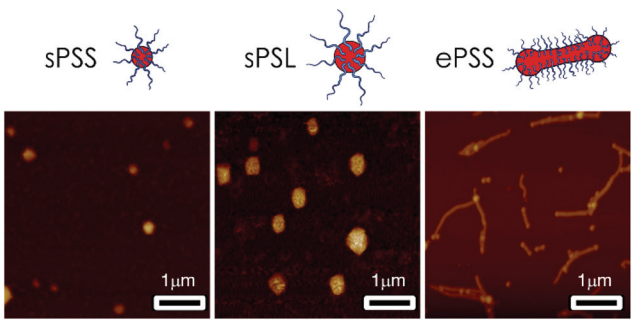

Fig. 1 Atomic Force Microscopy semi-contact topography scan of the three micelles. The diameter of the micelles is obtained from the full width at half maximum of the cross section from topography scans. Scale bar 1 μm.

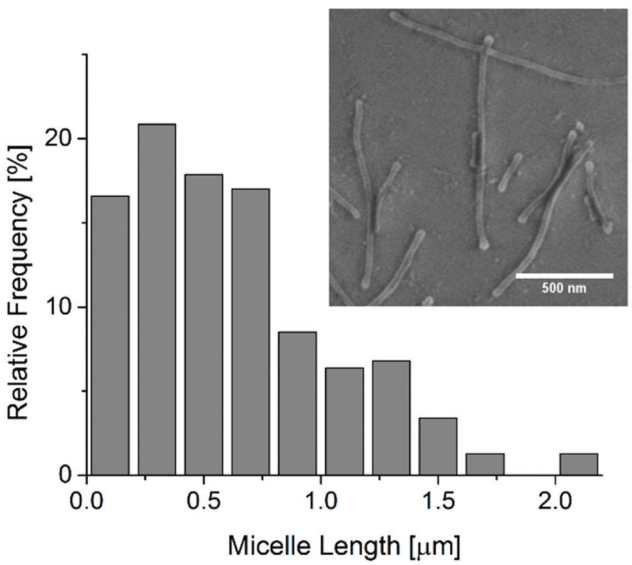

Fig. 2 Length distribution of ePSS micelles after homogenization. The longest micelles are fractured into many shorter ones. The lengths were measured from SEM micrographs like the one shown in the inset.

There was no visible effect of micelle cytotoxicity *in vitro* using concentrations up to 5 mg mL^{-1}, which was more than double the concentration used for our *in vivo* studies. This shows how the PS-PEO micelles can be used as a tool to explore possible morphology related improvements to existing therapies.

In vitro cellular internalization of PS-PEO micelles

Micelles were loaded with the fluorescent dye DiI to track their internalization in HeLa cells. This fluorophore is known to be efficiently retained in the hydrophobic core of block copolymer micelles.[28] The average fluorescence per cell was determined from confocal micrographs and is related to the total amount of fluorescent dye internalized by the cells. The results are shown in Fig. 3.

The results show that within the first hour of incubation the smaller spherical micelles, DiI-sPSS, are most rapidly internalized by the cells. After four hours of incubation both spherical micelles show the same levels of internalization while the elongated micelles, DiI-ePSS, are lagging behind. This can be due to the relatively large length distribution of the DiI-ePSS: the micelles on the shorter side of the length distribution behave similarly to large spherical micelles. However, the fraction of longer elongated micelles will be adhering to the cells and internalized through slower pathways.[29] After 12 hours of incubation time the total amount of fluorescence in the cells is approximately the same for all three micelle types. These results are very similar to those obtained by Shao *et al.* using active fluorescent nanoprobes.[30] The apparently faster rate of internalization of the DiI-ePSS in the later stages of internalization is explained by the fact that the longer micelles, while being internalized slower, also encapsulate larger amounts of DiI dye per micelle resulting in a higher amount of internalized dye within the cells. The higher loading capacity of elongated micelles with respect to spherical ones has been shown to be one of their major advantages when using them as drug carriers.[4,10]

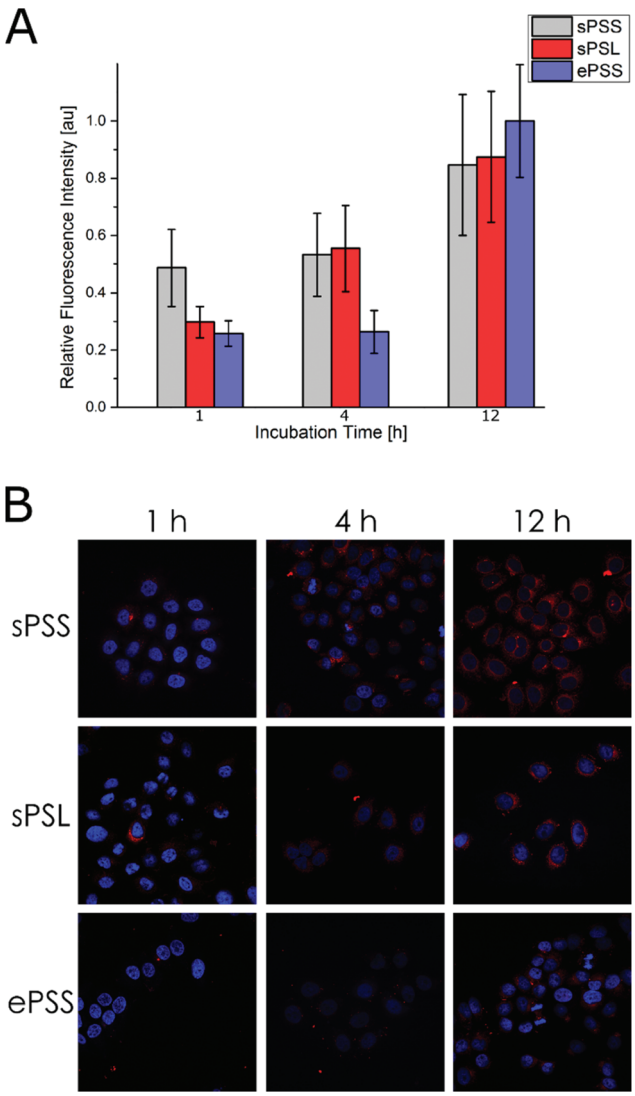

Fig. 3 A, Internalization of spherical and elongated fluorescently micelles in HeLa cells. The fluorescence was measured from CLSM images, such as those in figure B, and averaged per cell. The results are normalized relatively to the maximum fluorescence measured. The elongated micelles, ePSS, appear to be internalized at two different rates. A faster rate, comparable with that of the larger spherical micelles, and a slower one, which however results in a larger delivery of fluorescent dye to the cells.

Radiolabeling and purification of PS-PEO micelles

In order to study their circulation time and biodistribution in healthy mice, the micelles were radiolabeled with ^{111}In to obtain gamma-emitting carriers for SPECT imaging. The method used to encapsulate the radioisotope ^{111}In in the core of the micelles is based on the method developed by Laan *et al.*[31] where the isotope is complexed with the lipophilic chelator tropolone. Tropolone is a water-soluble, weakly negatively charged molecule which forms lipophilic complexes with the positively charged ^{111}In (oxidation state of 3+) in water solution at pH 7.4. These lipophilic complexes migrate to the chloroform phase during the evaporation of the emulsion that is required for the formation of the micelles. As the chloroform evaporates, the complex will be entrapped in the hydrophobic core of the micelles. The encapsulation efficiency depends on the partition of indium–tropolone complexes between the aqueous and organic phases of the emulsion. The unencapsulated ^{111}In is separated from the radiolabeled micelles using size exclusion chromatography. The elution profiles are shown in Fig. 4.

Free ^{111}In-tropolone is shown as a control. By selecting the elution fractions 3 to 5, all the free ^{111}In is excluded from the micelle solution. The total radiolabeling efficiencies are shown in Table S1 (ESI†). No changes in size were found when characterizing the plain micelles and the radiolabeled ones.

The radiolabeling efficiency of the technique used is related to the partition of the indium–tropolone complexes between the water phase and the chloroform phase prior micelle formation. While the efficiency obtained herein can potentially be optimized through formulation studies, it is outside the scope of this paper.

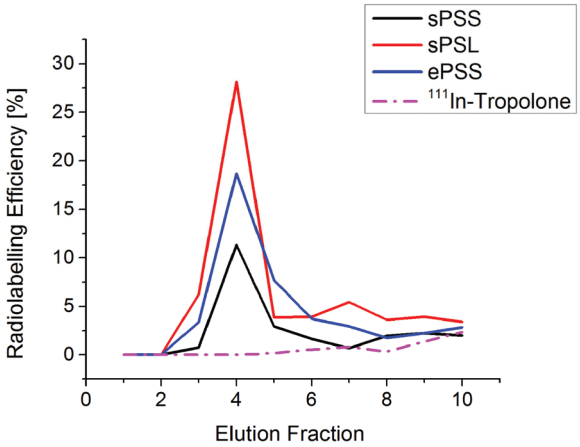

Fig. 4 Elution profile of the ^{111}In-labeled micelles. Free ^{111}In-tropolone is used as a control. In the first five fractions the micelles are eluted while free ^{111}In-tropolone is retained in the column.

In vivo biodistribution of PS-PEO micelles

In vivo SPECT studies were performed to assess the morphology-dependence of *in vivo* biokinetics and blood circulation of the micelles. Quantitative *in vivo* SPECT imaging has been chosen over blood sampling as a non-invasive evaluation of the circulation time. This has been done to not affect the animal's welfare[32,33] and, additionally, to not influence the residual concentration of radiopharmaceutical compounds in the blood stream which may affect the biodistribution of long-circulating radiopharmaceutical compounds during longitudinal studies. Moreover, with respect to organ internalization, it has been shown that quantitative SPECT measurements only deviate by less than 2.8% from gamma-counter measurements for ^{111}In, therefore proving that SPECT is currently the ideal technique for non-invasive longitudinal studies.[22,34,35]

Fig. 5A and Video S1–S3† show the maximum intensity projections of follow-up total body SPECT/CT scans for three mice, depicting the longitudinal changes in the biodistribution of ^{111}In-sPSS (top), ^{111}In-sPSL (middle) and ^{111}In-ePSS (bottom) micelles. At the same time, quantified uptake of the compound in multiple organs of interest (Fig. 5B, Table S2 and S3†) provides an absolute quantitative measure of the micelle distribution in the tissue.

Our results show (Fig. 5) that all nanocarriers have a high blood activity concentration (17.6 ± 3.6%ID mL^{-1} ^{111}In-sPSS, 17.4 ± 6%ID mL^{-1} ^{111}In-sPSL, 15.0 ± 3.6%ID mL^{-1} ^{111}In-ePSS, based on heart uptake values) and rapid spleen uptake (12.2 ± 4.3%ID mL^{-1} ^{111}In-sPSS, 11.0 ± 1.3%ID mL^{-1} ^{111}In-sPSL, 24.7 ± 0.4%ID mL^{-1} ^{111}In-ePSS) during early stage of the experiment. At the same time, the presence of a renal shell image at 0 hours p.i. scans suggests fast renal clearance of the compounds. However, the near absence of bladder activity accumulation by the end of 0 hours p.i. scans (*i.e.* 30 minutes p.i.) and the remaining renal cortex shell image on the later stage scans (24 and 48 hours p.i.) suggest an entrapment of the micelles in the renal cortex tissue. This interpretation is consistent with the value of kidney uptake on quantification plots (Fig. 5B) which remained almost constant during the two days of follow-up studies.

SPECT images at 24 hours p.i. show high level of activity elimination from the main vessels and the heart (6.1 ± 2.2%ID mL^{-1} ^{111}In-sPSS, 4.2 ± 0.6%ID mL^{-1} ^{111}In-sPSL, 4.6 ± 1.3%ID mL^{-1} ^{111}In-ePSS) of the animals, that is later followed by total clearance of the compounds from the blood, to the level of background signal, prior 48 hours p.i. imaging ($r > 0.99$ for all compounds).

The liver and spleen uptake become more prominent with time: ^{111}In-sPSL and ^{111}In-ePSS show very similar dynamics of spleen uptake ($r > 0.99$), yet have different rates of indium decomposition. For the ^{111}In-sPSL there is an increase of 3.3 times in the spleen uptake, from 0 to 24 hours p.i., while for the ^{111}In-ePSS the increase is 2.6 times. Liver accumulation of ^{111}In-sPSS micelles remains almost constant during two days of imaging, while a small increase in spleen accumulation (12.2 ± 4.4, 14.3 ± 1.8 and 17.3 ± 0.9%ID mL^{-1} at 0, 24 and 48 hours p.i.) is observed. Micelles of spherical morphology, ^{111}In-sPSS and ^{111}In-sPSL, showed similar dynamics of liver uptake ($r = 0.94$).

Fused SPECT/CT slices of 48 hours p.i. scans focused on the abdominal area of the animal (Fig. 6) show, in detail, the late stage biodistribution of ^{111}In-sPSS (top), ^{111}In-sPSL (middle) and ^{111}In-ePSS (bottom) micelles. Closer examination of the activity distribution on the coronal slices (Fig. S2–S4†) reveals a relatively high level of ^{111}In uptake within the liver which appears to be distributed homogeneously for the ^{111}In-sPSS micelles and increasingly heterogeneously going from the ^{111}In-sPSL to the ^{111}In-ePSS which also showed some liver clearance.

It was previously reported that micelles of elongated morphology, when compared to their spherical analogues, can have high brain and/or lungs uptake.[3] However, the brain uptake of the elongated ^{111}In-ePSS micelles studied in this work (1.9 ± 0.3%ID mL^{-1} ^{111}In-ePSS at 0 h p.i., Table S2†) had no significant difference with the uptake of spherical micelles (1.8 ± 0.4%ID mL^{-1} ^{111}In-sPSS, 1.7 ± 0.1%ID mL^{-1} sPSL at 0 h p.i.). Moreover, although we saw a high activity concentration in lungs (13.6 ± 2.1%ID mL^{-1} ^{111}In-sPSS, 13.2 ± 1.2%ID mL^{-1} ^{111}In-sPSL and 10.6 ± 3.0%ID mL^{-1} ^{111}In-ePSS; Table S2†) at the early stage of the experiment (0 h p.i.), this value significantly decreased over imaging days (4.5 ± 1.2%ID mL^{-1} ^{111}In-sPSS, 3.1 ± 0.3 ^{111}In-sPSL, 3.4 ± 1.0 ^{111}In-ePSS at 24 h p.i.). In this case, the initial high activity concentration in the lungs, is probably associated with the relatively high perfusion of the lungs (~4.5 time higher than in liver),[36] while the gradual decrease in lungs activity concentration indicates that none of the compounds is being trapped in the organ. For all compounds studied, negligible activity was accumulated in the skeleton of the animals (Fig. 5). This indicates that minimal dissociation of ^{111}In in its ionic form from the carriers after i.v. administration.[37–39] This statement is consistent with the previously reported mouse serum stability tests for ^{111}In-labelled micelles equivalent to the ones used in our experiments.[31]

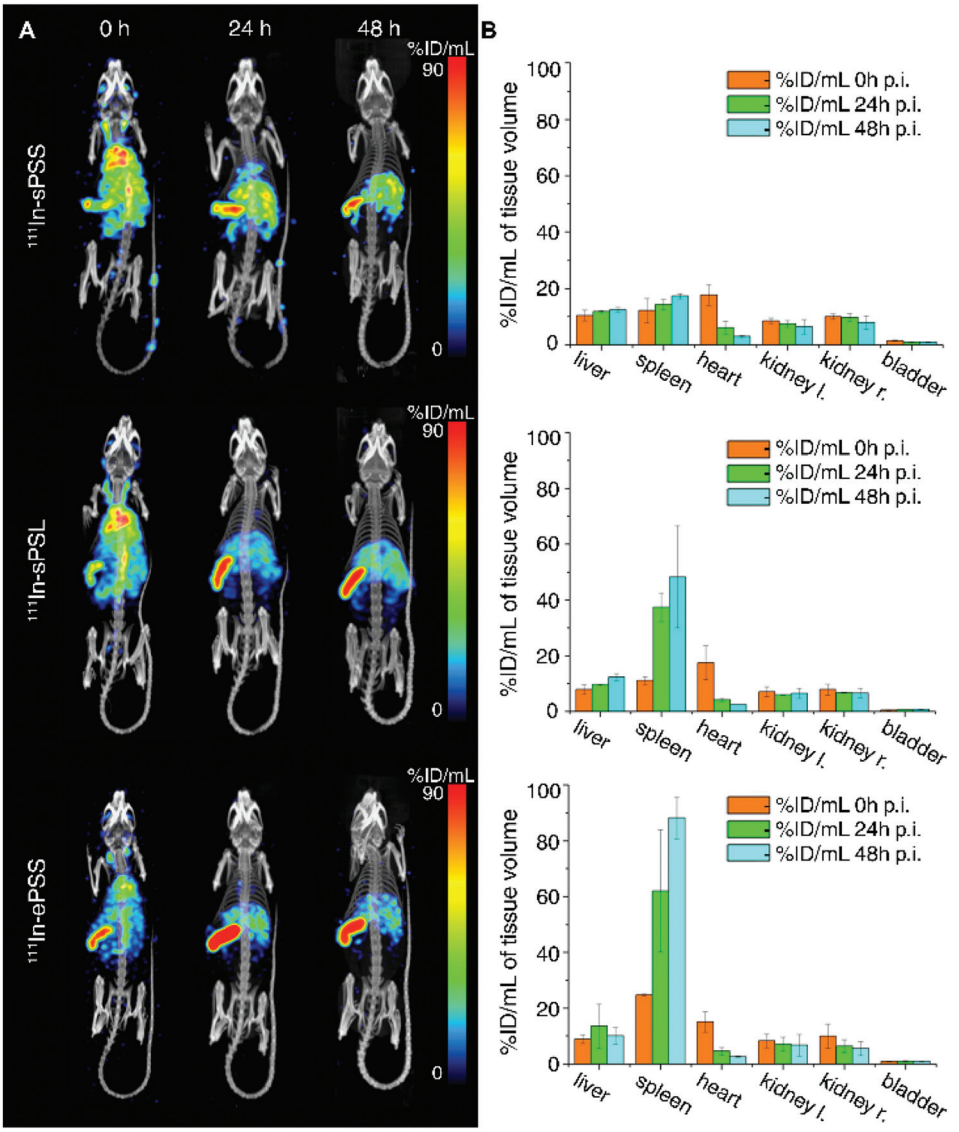

Fig. 5 A – Maximum intensity projections of follow-up SPECT/CT scans of three mice at 0, 24 and 48 hours post injection of ^{111}In-sPSS (top), ^{111}In-sPSL (middle) or ^{111}In-ePSS (bottom) compound respectively. B – quantified uptake of the compounds in multiple organs of interest, calculated from corresponding SPECT/CT scans.

Discussion

In this work we studied the effects of the shape, size and rigidity of PS-PEO micelles on their circulation time, general biodistribution and clearance pathways in mice.

Spherical and elongated micelles of polystyrene-*b*-poly(ethylene oxide) were prepared using a co-solvent evaporation method which made it possible to physically encapsulate a hydrophobic fluorescent dye or complexed radioisotopes from the micelle formation stage without altering their surface properties.

From *in vitro* cellular internalization experiments with HeLa cells it was found that the internalization rate of the micelles depends on their morphology. In contrast to micelles of spherical morphology (sPSS d = 120 nm and sPSL d = 190 nm), that showed approximately constant rate of cellular internalization over 12 hours, the elongated micelles (ePSS 30 × 600 nm) appear to be internalized at two different rates. The initial phase is characterized by slow rate of cellular internalization (up to 4 hours) and the late phase has a fast uptake. However, when compared to spherical micelles, both uptake rates of ePSS result in a larger delivery of fluorescent dye to the cells. In this case, the higher loading capacity of elongated micelles with respect to spherical ones illustrates one of their major advantages as drug carriers.[4,10] Moreover, no cytotoxic effects for the different micelle morphologies were found for concentrations up to 5 mg mL^{-1} which was more than double the concentration used for *in vivo* studies.

Next, the micelles were radiolabelled with ^{111}In and we studied their biodistribution in healthy mice. Overall, the

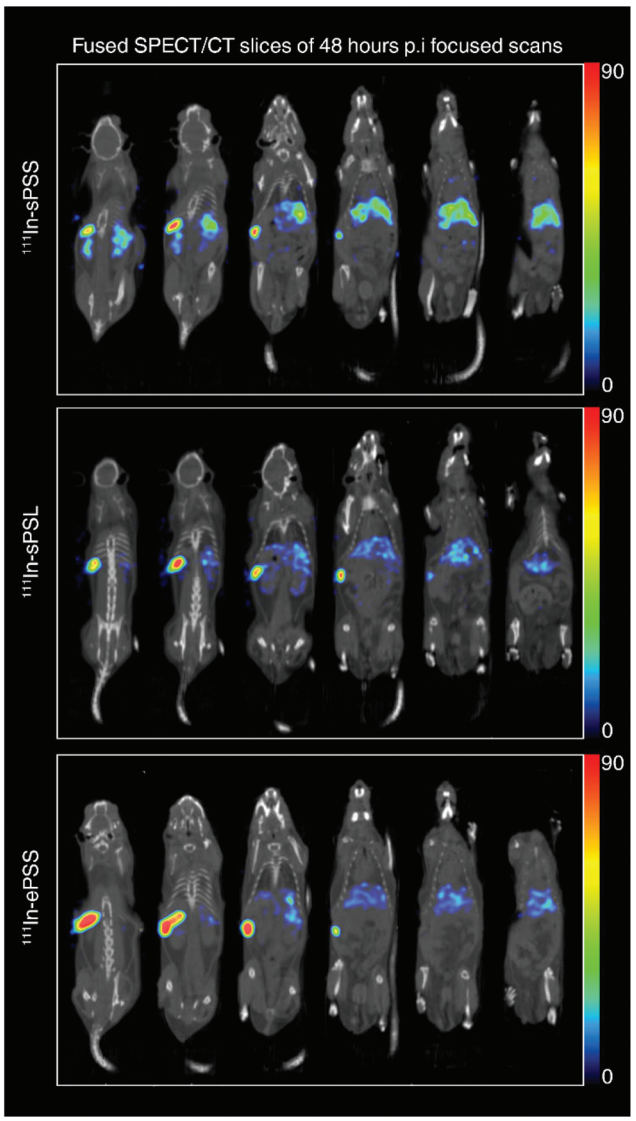

Fig. 6 Fused SPECT/CT slices of focused abdominal area scans (right) at 48 hours post injection of ^{111}In-sPSS (top), ^{111}In-sPSL (middle) or ^{111}In-ePSS (bottom) compound respectively.

major site of accumulation for all compounds studied was the spleen. Regarding the circulation time, our results demonstrated that the carrier with the fastest initial clearance is ^{111}In-ePSS. The carrier with the longest circulation time is ^{111}In-sPSS which showed the highest %ID mL^{-1} heart uptake value (Fig. 5B) in the 24 hours p.i. scan. This value represents an average activity concentration in the blood passing through the heart. ^{111}In-sPSL and ^{111}In-ePSS showed slightly lower heart uptake values at 24 hours p.i. (Fig. 5B, Table S2†), but all three morphologies show no statistical difference in blood activity concentration at 48 hours p.i. Furthermore, a significant late stage increase in spleen uptake of ^{111}In-sPSL and ^{111}In-ePSS (Fig. 5B) suggests a circulation time of the compounds that is longer than 24 hours. These results correlate with previously reported long circulation times for PS-PEO micelles and suggest a good potential for EPR effect related investigation.[24] However, based on our results we can state that the high aspect ratio of PS-PEO elongated micelles does not provide an increased circulation time. This is especially different from the order of magnitude increase in circulation time that was previously reported by Geng *et al.* for the PEO-PCL filomicelles.[4,10] Our results are more closely related to those obtained by Müllner *et al.*, who used high molecular weight brush copolymers to study their circulation time and biodistribution while varying the length and rigidity of the backbone.[11] The authors showed that an increased length results in an increased splenic capture, while an increased rigidity results in a faster clearance. The aspect of rigidity was also confirmed recently by Anselmo *et al.* who showed using spherical hydrogel nanoparticles that the circulation time decreases with increasing rigidity of the particles.[40] From this we can conclude that for micelles with a stiff core, such as the polystyrene based ones used in this work, the circulation time is longer for spherical particles rather than elongated ones.

Finally, we can summarize the difference in longitudinal *in vivo* biodistribution of the three micelle types through their differences in size and morphology. The general trend observed is that the PS-PEO nanocarriers accumulate in the spleen, liver and renal cortex. The nanocarriers with larger characteristic dimensions accumulate preferentially in the spleen, while the smallest are divided equally between spleen and liver. Nanoparticles which are larger than 100 nm have been shown to preferentially accumulate in the spleen rather than the liver which is consistent with our results with the spherical micelles.[41] Moreover, stiffer carriers have also been reported to accumulate preferentially in the spleen rather than the liver.[36] As a result of the combination of their sizes and stiffness, given by the polystyrene core, the elongated micelles show a remarkably specific spleen uptake. As previously mentioned, the splenic accumulation of the larger micelles is consistent with the results shown for high molecular cylindrical polymer brushes.[11] Since the spleen is the primary organ of the immune system this result could lead to interesting applications, for example in the field of vaccine delivery.[42] At the same time, it must be noted that our experiments were carried out on an animal model (C57Bl/6 mouse) with non-sinusoidal spleen, while both rat and human spleens have a sinusoidal structure. The sinusoidal sleeves provide an extra layer of filtration for carriers which have high rigidity, sizes larger than 200 nm and elongated shapes.[43,44] Regarding the liver, the Kupffer cells are responsible for the internalization of nanoparticles. These are known to have a rough surface which promotes phagocytosis of particles with a diameter between 1 and 3 μm.[2,29] The carrier which mostly represents this range are the elongated micelles ePSS along their long axis. However, our results show that the small spherical particles are being preferentially uptaken in the liver. This is again likely due to the rigidity of the elongated micelles which promotes their spleen uptake and indirectly contributes to a reduction of the accumulation in the liver.

Conclusions

Spherical and elongated micelles of polystyrene-*b*-poly(ethylene oxide) were prepared using a co-solvent evaporation method which made it possible to physically encapsulate a hydrophobic dye or complexed radioisotopes from the micelle formation stage. This theranostic device shows great versatility for research purposes since markers, as long as hydrophobic, can potentially be encapsulated without costly formulation efforts and without influencing the surface properties of the carriers. From these experiments it was found that the internalization rate of the micelles depends on their morphology. Moreover, no cytotoxic effects for the different micelle morphologies were found for concentrations up to 5 mg mL^{-1}.

The micelles mainly distributed between liver and spleen for all the three samples tested. The size increase of spherical micelles influenced their rates of spleen accumulation without any obvious effect of general liver uptake. The elongated micelles showed a delayed liver clearance and a remarkably specific accumulation in the spleen which is explained by their morphology coupled with the stiffness of the core forming block. Finally, the shorter circulation time of the elongated micelles, caused by their rigid core, highlights the importance of describing elongated micelles not only as a function of their size, but also of their mechanical properties. Further studies using non degradable elongated micelles of different stiffness, and therefore persistence length, are necessary in order to further clarify the aspect of morphology related biodistribution and circulation time.

Author contribution

The manuscript was written through contributions of all authors. All authors have given approval to the final version of the manuscript.

Acknowledgements

The research leading to these results has received funding from the People Programme (Marie Curie Actions) of the European Union's Seventh Framework Programme (FP7/2007–2013) under REA grant agreement no. PITN-GA-2012-317019 'TRACE 'n TREAT.

Notes and references

1 P. Decuzzi and M. Ferrari, *Biomaterials*, 2006, **27**, 5307–5314.
2 J. A. Champion and S. Mitragotri, *Proc. Natl. Acad. Sci. U. S. A.*, 2006, **103**, 4930–4934.
3 P. Kolhar, A. C. Anselmo, V. Gupta, K. Pant, B. Prabhakarpandian, E. Ruoslahti and S. Mitragotri, *Proc. Natl. Acad. Sci. U. S. A.*, 2013, **110**, 10753–10758.
4 Y. Geng, P. Dalhaimer, S. Cai, R. Tsai, M. Tewari, T. Minko and D. E. Discher, *Nat. Nanotechnol.*, 2007, **2**, 249–255.
5 T. Mustonen and K. Alitalo, *J. Cell Biol.*, 1995, **129**, 895–898.
6 H. F. Dvorak, J. A. Nagy, D. Feng, L. F. Brown and A. M. Dvorak, *Curr. Top. Microbiol. Immunol.*, 1999, **237**, 97–132.
7 H. Maeda, *Adv. Enzyme Regul.*, 2001, **41**, 189–207.
8 H. Maeda, J. Wu, T. Sawa, Y. Matsumura and K. Hori, *J. Controlled Release*, 2000, **65**, 271–284.
9 Y. Geng and D. E. Discher, *J. Am. Chem. Soc.*, 2005, **127**, 12780–12781.
10 D. a. Christian, S. Cai, O. B. Garbuzenko, T. Harada, A. L. Zajac, T. Minko and D. E. Discher, *Mol. Pharm.*, 2009, **6**, 1343–1352.
11 M. Müllner, S. J. Dodds, T. H. Nguyen, D. Senyschyn, C. J. H. Porter, B. J. Boyd and F. Caruso, *ACS Nano*, 2015, **9**, 1294–1304.
12 Y. M. Wang, C. M. Kausch, M. S. Chun, R. P. Quirk and W. L. Mattice, *Macromolecules*, 1995, **28**, 904–911.
13 S. Jain and F. S. Bates, *Macromolecules*, 2004, **37**, 1511–1523.
14 C. Allen, D. Maysinger and A. Eisenberg, *Colloids Surf., B*, 1999, **16**, 3–27.
15 J. Zhu and R. C. Hayward, *J. Am. Chem. Soc.*, 2008, **130**, 7496–7502.
16 K. Yu and A. Eisenberg, *Macromolecules*, 1996, **29**, 6359–6361.
17 F. van der Have, B. Vastenhouw, R. M. Ramakers, W. Branderhorst, J. O. Krah, C. Ji, S. G. Staelens and F. J. Beekman, *J. Nucl. Med.*, 2009, **50**, 599–605.
18 O. Ivashchenko, F. van der Have, M. Goorden, R. M. Ramakers and F. J. Beekman, *J. Nucl. Med.*, 2015, **56**, 470–476.
19 W. Branderhorst, B. Vastenhouw and F. J. Beekman, *Phys. Med. Biol.*, 2010, **55**, 2023–2034.
20 F. Van Der Have, B. Vastenhouw, M. Rentmeester and F. J. Beekman, *IEEE Trans. Med. Imaging*, 2008, **27**, 960–971.
21 M. A. King, S. J. Glick, P. H. Pretorius, R. G. Wells, H. C. Gifford, M. V. Narayanan and T. Farncombe, *Emiss. Tomogr.*, Acad. Press, San Diego, 2004.
22 C. Wu, J. R. de Jong, H. A. Gratama van Andel, F. van der Have, B. Vastenhouw, P. Laverman, O. C. Boerman, R. A. J. O. Dierckx and F. J. Beekman, *Phys. Med. Biol.*, 2011, **56**, N183–N193.
23 M. Su and Z. Su, *Macromolecules*, 2014, **47**, 1428–1432.
24 S. M. D'Addio, W. Saad, S. M. Ansell, J. J. Squiers, D. H. Adamson, M. Herrera-Alonso, A. R. Wohl, T. R. Hoye, C. W. MacOsko, L. D. Mayer, C. Vauthier and R. K. Prud'homme, *J. Controlled Release*, 2012, **162**, 208–217.
25 G. Jia, H. Wang, L. Yan, X. Wang, R. Pei, T. Yan, Y. Zhao and X. Guo, *Environ. Sci. Technol.*, 2005, **39**, 1378–1383.
26 Y. Zhang, D. Xu, W. Li, J. Yu and Y. Chen, *J. Nanomater.*, 2012, **2012**, 1–7.
27 X. Zhao, S. Ng, B. C. Heng, J. Guo, L. Ma, T. T. Y. Tan, K. W. Ng and S. C. J. Loo, *Arch. Toxicol.*, 2013, **87**, 1037–1052.

28 A. Mahmud and A. Lavasanifar, *Colloids Surf., B*, 2005, **45**, 82–89.
29 N. Doshi and S. Mitragotri, *PLoS One*, 2010, **5**, 1–6.
30 A. Shao, Y. Xie, S. Zhu, Z. Guo, S. Zhu, J. Guo, P. Shi, T. D. James, H. Tian and W. H. Zhu, *Angew. Chem., Int. Ed.*, 2015, 7275–7280.
31 A. C. Laan, C. Santini, L. Jennings, M. de Jong, M. R. Bernsen and A. G. Denkova, *EJNMMI Res.*, 2016, **6**, 12.
32 H. Holmberg, M. K. Kiersgaard, L. F. Mikkelsen and M. Tranholm, *Lab. Anim.*, 2011, **45**, 114–120.
33 P.-P. Tsai, A. Schlichtig, E. Ziegler, H. Ernst, J. Haberstroh, H. D. Stelzer and H. Hackbarth, *Lab Anim.*, 2015, **44**, 301–310.
34 C. Wu, F. van der Have, B. Vastenhouw, R. A. J. O. Dierckx, A. M. J. Paans and F. J. Beekman, *Eur. J. Nucl. Med. Mol. Imaging*, 2010, **37**, 2127–2135.
35 C. M. Finucane, I. Murray, J. K. Sosabowski, J. M. Foster and S. J. Mather, *Int. J. Mol. Imaging*, 2011, **2011**, 1–8.
36 N. Bertrand and J. C. Leroux, *J. Controlled Release*, 2012, **161**, 152–163.
37 F. Hosain, P. A. McIntyre, K. Poulose, H. S. Stern and H. N. Wagner, *Clin. Chim. Acta*, 1969, **24**, 69–75.
38 M. H. Adatepe, P. Penkoske, A. Van Amberg, T. Wharton, R. G. Evens and E. J. Potchen, *Int. J. Appl. Radiat. Isot.*, 1971, **22**, 498–501.
39 Y. Ohtake, A. Maruko, S. Satoh and Y. Ohkubo, *Appl. Radiat. Isot.*, 2008, **66**, 1245–1249.
40 A. C. Anselmo, M. Zhang, S. Kumar, D. R. Vogus, S. Menegatti, M. E. Helgeson and S. Mitragotri, *ACS Nano*, 2015, **9**, 3169–3177.
41 X. Duan and Y. Li, *Small*, 2013, **9**, 1521–1532.
42 Y. Yang, T. Neef, C. Mittelholzer, E. Garcia Garayoa, P. Bläuenstein, R. Schibli, U. Aebi and P. Burkhard, *J. Nanobiotechnol.*, 2013, **11**, 36.
43 M. Demoy, J. P. Andreux, C. Weingarten, B. Gouritin, V. Guilloux and P. Couvreur, *Pharm. Res.*, 1999, **16**, 37–41.
44 Z. Liu, C. Davis, W. Cai, L. He, X. Chen and H. Dai, *Proc. Natl. Acad. Sci. U. S. A.*, 2008, **105**, 1410–1415.

